AIMS Materials Science, 11(1): 28–57.
DOI: 10.3934/matersci.2024002
Received: 02 October 2023
Revised: 01 December 2023
Accepted: 07 December 2023
Published: 25 December 2023

http://www.aimspress.com/journal/Materials

*Research article*

# A study on the static behavior of functionally graded I-shaped beams

**M.A.R. Loja[1,2,*], André Carvalho[1,2] and Ines C.J. Barbosa[1,2]**

[1] CIMOSM, Centro de Investigação em Modelação e Otimização de Sistemas Multifuncionais, ISEL/IPL, Instituto Superior de Engenharia de Lisboa, Av. Conselheiro Emídio Navarro 1, 1959-007 Lisboa, Portugal
[2] IDMEC, IST-Instituto Superior Técnico, Universidade de Lisboa, Av. Rovisco Pais, 1, 1049-001 Lisboa, Portugal

* **Correspondence:** Email: amelia.loja@isel.pt; Tel: +351-218317000.

**Abstract:** Functionally graded materials are well-known for their ability to minimize abrupt stress transitions that are typical of laminated composites, as well as for being very suitable to operate in adverse high-temperature environments. They can act as thermal barriers if a proper selection of the constituent materials is considered. These materials and structures have attracted the attention of many researchers; however, previous research efforts have been focused on the systematic study of rectangular-shaped cross-section profiles. The use of beams characterized by other cross-sections, which are commonly used in metallic construction, may benefit from the continuous, smooth materials mixture that is typically found within functionally graded composites. Hence, this work aims to investigate the behavior of symmetrical, I-shaped, cross-section beams made from these advanced composites by performing a set of parametric analyses. These beams are modeled after solid finite elements to be able to describe the materials mixture evolution through the beam thickness with greater detail. Thick and moderately thick beams are submitted to static loading while considering different boundary conditions, and their linear static behavior is analyzed. As expected, the stress profiles are highly influenced by the materials' mixture profiles. Significant shear stress was found in the I-shaped cross sections.

**Keywords:** functionally graded materials; symmetric I-shaped cross-section beams; finite element method

## 1. Introduction

Previously, there has been a widespread use of homogenous materials. Nowadays, numerous applications require manufactured materials; therefore, there has been a gradual change in composition and structure. To achieve this gradual distribution of material properties, new heterogeneous composite materials with multi-functional characteristics, formally known as functionally graded materials (FGM), were designed.

These materials are composite materials, containing at least two different materials, whose volume fraction gradually changes along one or more dimensions of the solid [1]. This gives FGMs a continuously varying composition and structure over the volume of the component or entity, which results in varying properties for the material. Thus, FGMs are engineered to perform in specific applications that require certain desired thermal, mechanical, electrical, or chemical properties [2–4]. Additionally, due to their gradually changing properties, FGMs have interesting characteristics such as improved thermal properties, an enhanced residual stress distribution, reduced in-plane and traverse stresses over their thickness, and an enhanced fracture resistance [5].

Due to these characteristics, many researchers have been interested in FGMs. For example, the review written by Garg et al. [4] presented information on theories and methods mainly used to perform an analysis of FGMs, such as the classical laminated theory, the first-order shear deformation theory, and various higher-order shear deformation theories. Additionally, was shown that the most static and dynamic analyses were performed using the finite element (FE) method. However, Sayyad and Ghugal [2], who also reviewed the modeling and analysis of FGMs, presented several works on FGMs sandwich beams. They found that the power law was utilized the most to model the varying properties of FGMs. The authors presented several numerical and analytical studies and claimed that there was no available exact elasticity solution for FG beams with varying material properties. Additionally, they claimed that an increased emphasis should be placed on analytical solutions based on higher-order theories that consider transverse shear and normal deformations.

In the analysis of FGMs, Kanu et al. [6] considered that some authors tried to introduce new methods to improve 3D analyses; however, due to a collective computational effort, most researchers opted for 2D analyses of FGMs using higher-order shear deformation theories. This restriction compromised the accuracy of the obtained results. Thus, other methods, such as the meshless method, were used as an alternative to the FE method, though they were highly time-consuming. In their review, the FGM manufacturing process was also considered alongside other various processes. Powder metallurgy was thought to be the most efficient method to manufacture FGMs; however, more research on the sintering process was advised to improve the mechanical properties and the microstructure of the product.

Regarding the manufacturing of FGMs, other authors focused on understanding which processes were better for each application, and a list of recommendations was written to decide on the most adequate manufacturing process to successfully fabricate FGMs [5]. Additive manufacturing seems to be the best method to further improve the production of dual gradient or hybrid FGMs at a lower cost [3].

In terms of the mechanical properties of FGMs, there are several researchers who analyze beams. Single layer FGMs are the most studied, though the development of multi-layered FGMs has also become an object of research [7–10]. Additionally, researchers have analyzed the application of a single layer approach that focuses on thin-walled FGMs [11–13].

Regarding the study of FGM beams, Filippi et al. [14] performed different static analyses on beam

FEs based on various displacement theories and determined that the Carrera Unified Formulation performed very well and was able to consider different supporting and loading conditions, as well as arbitrary material distributions and dimensions. The main difficulty encountered was obtaining accurate shear stress distributions. It was proposed that higher-order beam theories may improve these results, although with higher computational costs. To improve the performance of FE analyses on FGMs, new elements and methods are being studied to more accurately model the gradient distribution and to obtain better mechanical properties [15–22].

There have been several studies on the nonlocal behavior of nanobeams. Among those works, one may refer to the investigation carried out by Penna et al. [23], where the nonlinear transverse free vibrations of porous FGM Bernoulli-Euler nanobeams in hygrothermal environments through the local/nonlocal stress gradient theory of elasticity were studied. In more recent work, Penna [24] analyzed the bending response of FGM Bernoulli-Euler nanobeams with rectangular and circular cross-section shapes using a stress-driven model incorporating surface energy effects. Following this work and based on the same method, Lovisi [25] investigated the bending response of cracked FGM Bernoulli-Euler nanobeams by considering a one-dimensional simplified method in which a discontinuity in the rotation due to a crack in an internal point was modelled as a rotational spring connecting two segments, into which the cracked FG nanobeam was divided. Additionally, in the context of the nonlocal approaches, Loja et al. [26] studied the free-vibration response of functionally graded, simply supported beams with different gradient directions by considering nonlocal effects. To this purpose, the authors used the first-order shear deformation theory and the nonlocal elasticity theory of Eringen to assess the influence of size dependency effects on the free-vibration responses of those beams.

Moreover, many researchers have studied the influence of hygrothermal loads. Among others, one may refer to the work of Giunta et al. [27], who analyzed functionally graded beams subjected to thermal loadings via a Navier-type closed-form. The authors hierarchically derived several beam models using a unified formulation that made the formulation independent from the displacement's polynomial approximation order over the cross-section. Fourier's heat conduction equation was used to obtain the temperature profile, which is the temperature of an externally applied load. Qin et al. [28] studied the flap-wise free vibrational characteristics of a rotating composite beam under an aerodynamic force and a hygrothermal environment. The modal problem was handled by utilizing the assumed-modes method, and the influence of parameters such as the temperature, humidity, aerodynamic force, rotational speed, ply orientation on the natural frequencies, and damping ratios were also investigated. A finite element model based on Reddy's third-order shear deformation theory was considered by Valencia et al. [29] to perform thermal-structural analyses of FGM beams subjected to thermal and mechanical loads. The constituent materials of the FGM varied throughout the direction of the beam thickness, and considered the power law and the rule of mixtures. Additionally, the authors used a routine to study functionally graded plane models in a commercial finite element code for verification purposes.

Other studies focused on the influence of porosities on the structural responses. For example, Tian et al. [30] presented a semi-analytical model for a free vibration analysis of rotating FGM beams with porosities and a double-tapered cross-section. The proposed model considered the Coriolis and nonlinear effects which arose from the interaction among various vibration modes, such as bending-stretching, bending-twist and twist-stretching couplings. Mota et al. [31] analyzed the influence of the shear correction factor on the static response of functionally graded porous composites via the first-order shear deformation theory. This work studied the influence of various porosity distributions on

various materials with a shear correction factor. Akbaş et al. [32] presented an additional model which investigated the vibrational response of FGM porous, thick beams subjected to a dynamic sine pulse load and damping [32]. In this study, the beam was modelled as a two-dimensional plane stress problem, with a material gradient throughout the thickness. Typical porosity distributions were assumed, and the damping effect was considered by using the Kelvin-Voigt viscoelastic constitutive model.

From the literature, it is very clear that most published studies on FGM beams focus on rectangular cross-section-shaped beams. Only some works were found that considered the non-uniformity of the cross-section shape; for example, Lee and Lee [33] investigated the coupled flexural-torsional free vibration of circular horizontally curved beams made of FGM along the axial direction. In this study, rectangular and elliptical cross-section beams were considered. The authors used the first-order shear deformation and the St. Venant beam theories to derive the governing differential equations of motion. The results were verified against the commercial software ADINA results. Özmen and Özhan [34] proposed a computational approach to model the material gradient of an FGM Euler-Bernoulli beam continuously according to graduation laws using the Ansys Workbench. This approach was applied to the free vibration analyses of different types of FGM beams, namely one-directional beams with a uniform and a non-uniform cross-section, and a bi-directional beam with a uniform cross-section. Li et al. [35] presented another approach to analyze the free vibration of FGM with variable cross-sections and rested on Pasternak elastic foundations. Displacements and general stress expressions were obtained using the separate variable method and the Laplace transform supported by the 2D elasticity theory. Frequency equations for free vibrations were derived by applying a Fourier series expansion. Parametric studies were developed to characterize the influence of geometric and mechanical parameters on the vibration frequency and the mode shapes of FGM beams with variable cross-sections resting on Pasternak elastic foundations. More recently, in the context of 2D plane FGM structures, Gaspar et al. [36] investigated the static and free vibration behavior of planar, truss and frame-type structures made from functionally graded materials, in which the materials' mixture gradient progressed along the height of the structures. For this purpose, the authors considered the use of the first-order shear deformation theory. Parametric studies were performed to characterize the advantages of such an approach, thereby showing that this may be considered as an additional design variable.

Regarding the use of cross-sections separate from rectangular ones, there is no sufficient evidence of published studies, even for other types of composites, as is the case of Loja et al. [37], who developed a model based on a higher-order shear-deformation theory to predict the linear buckling behavior of either anisotropic laminated or sandwich thick and thin beams. That higher-order model considered stretching and bending in two orthogonal planes: I, T, channel, and rectangular box beam cross-sections.

As far as the authors' knowledge, no published work was found that considered the use of functionally graded materials in I-shaped cross-sections of beam-bar components, although the common use of these shapes is in the context of structures built from traditional materials. As such, the main objective of this work is to perform linear static analyses of I-shaped cross-section FGM beams modelled by using 8-node hexahedron finite elements. Some verification cases are presented, and several parametric analyses characterize the influence of the material and geometric characteristics.

## 2. Materials and methods

### *2.1. Beam geometrical configuration*

The beam standard configuration that will be considered in the different case studies is shown in Figure 1. The geometry of this beam is defined by the top flange width $w_t$ the web thickness $t_w$ the bottom flange width $w_b$ the top flange's thickness $t_t$ the web height $h_w$ and the bottom flange's thickness $t_b$.

It is important to note the coordinate axes, with origin in the middle of the bottom of the beam, are oriented as follows: the height of the beam is measured in the z-axis, its width in the y-axis, and its length in the x-axis.

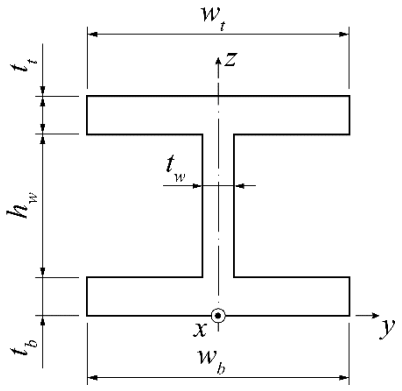


**Figure 1.** Beam cross-section geometry.

As mentioned, an FGM is a composite material wherein the materials' mixture involves a gradient micro-structure spatial variation from one material to another, which may occur in one or more directions [12,38]. In this work, the I-shaped cross-section beam is composed of two constituent materials, steel and alumina (aluminum oxide), with the properties presented in Table 1.

Table 1. Material properties.

| ID | Material | Young's Modulus (GPa) | Poisson's Coefficient |
|---|---|---|---|
| A | Alumina | 380 | 0.3 |
| B | Steel | 200 | 0.3 |

The following proposed volume fraction law, $V_f$ consists of a function with seven parameters to account for the gradation through the height of the cross-sectional area:

$$V_f = \begin{cases} 1 & 0 \le z \le z_{min} \\ \dfrac{(1-C_1)\left(\cosh\left(C_{2A}(z-z_{cutA})\right)-1\right)}{\cosh\left(C_{2A}(z_{min}-z_{cutA})\right)-1} + C_1 & z_{min} \le z \le z_{cutA} \\ C_1 & z_{cutA} \le z \le z_{cutB} \\ \dfrac{(1-C_1)\left(\cosh\left(C_{2B}(z-z_{cutB})\right)-1\right)}{\cosh\left(C_{2A}(z_{max}-z_{cutB})\right)-1} + C_1 & z_{cutB} \le z \le z_{max} \\ 1 & z_{max} \le z \le 1 \end{cases} \quad (1)$$

where $z$ is the thickness coordinate variable; $z_{min}$ and $z_{max}$ are the material saturation limits in the flanges' thickness; $z_{cutA}$ and $z_{cutB}$ are the material saturation limits in the web thickness; $C_1$ is the minimum quantity of the main material in the web; and $C_{2A}$ and $C_{2B}$ are controls for the transition between materials. In these variables, $A$ and $B$ represent the two materials involved in the gradient. To allow for a volume fraction distribution that considers the possibility of having a full functionally graded material cross-section, the values of $z_{min}$ and $z_{max}$ would be zero and one, respectively, thus eliminating the first and last branch.

For example, if the flanges that have a constant material distribution are considered, Figure 2 may be obtained. The volume fraction defined by Eq 1 is presented by the blue line for material A and by the red line for the material B, which is most present on the web is defined by a volume fraction function complementary to Eq 1. This is because the present FGM is a biphasic material with no porosities; therefore, the following relations apply:

$$\mathrm{V_{fA}} + \mathrm{V_{fB}} = 1 \tag{2}$$

$$P_{FGM} = \mathrm{V_f} P_A + (1 - \mathrm{V_f}) P_B \tag{3}$$

where $P_X$ stands for a generic property $P$ of material $X$.

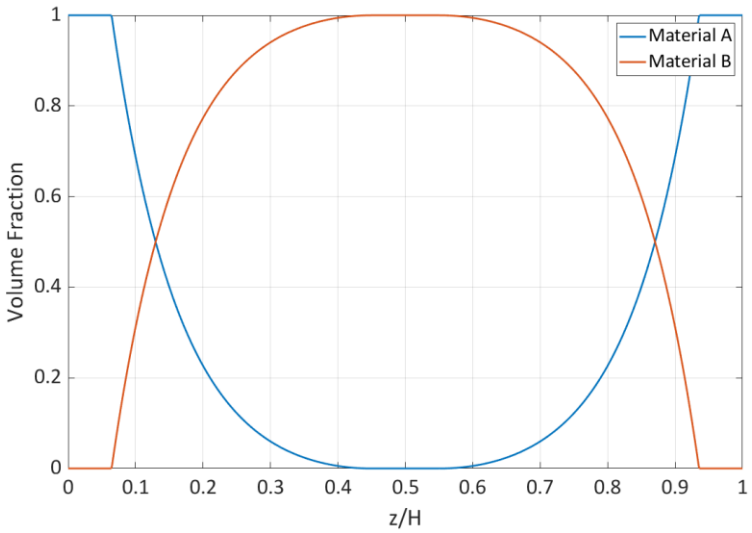


**Figure 2.** Volume fraction distribution.

### *2.2. Constitutive relations and equilibrium equations*

To achieve a more detailed description of the beams' kinematic deformation and the subsequent stress distributions, one can consider an approach based on the description of the movement of a generic point while considering its three displacement components, $u$, $v$ and $w$, along the 3D Cartesian coordinate system, $x$, $y$ and $z$.

From this point and considering the kinematic relations of the elasticity theory for small deformations, one obtains the strain field characterized by the standard six linear strain components:

$$\boldsymbol{\epsilon} = \left[\varepsilon_x, \varepsilon_y, \varepsilon_z, \gamma_{xy}, \gamma_{xz}, \gamma_{yz}\right]^T \tag{4}$$

As mentioned in the previous subsection, the utilized materials are a biphasic FGM. Based on the assumption that such material can be considered as an isotropic material at each point, the following constitutive relation applies and will relate the states of strain and stress at an arbitrary point (Reddy, [39]):

$$\begin{bmatrix} Q_{11}(z) & Q_{12}(z) & Q_{13}(z) & 0 & 0 & 0 \\ Q_{21}(z) & Q_{22}(z) & Q_{23}(z) & 0 & 0 & 0 \\ Q_{31}(z) & Q_{32}(z) & Q_{33}(z) & 0 & 0 & 0 \\ 0 & 0 & 0 & Q_{11}(z) & 0 & 0 \\ 0 & 0 & 0 & 0 & Q_{11}(z) & 0 \\ 0 & 0 & 0 & 0 & 0 & Q_{11}(z) \end{bmatrix} \begin{bmatrix} \varepsilon_x \\ \varepsilon_y \\ \varepsilon_z \\ \gamma_{xy} \\ \gamma_{xz} \\ \gamma_{yz} \end{bmatrix} = \begin{bmatrix} \sigma_x \\ \sigma_y \\ \sigma_z \\ \tau_{xy} \\ \tau_{xz} \\ \tau_{yz} \end{bmatrix} \tag{5}$$

$$\boldsymbol{Q\epsilon} = \boldsymbol{\sigma} \tag{6}$$

To develop a linear static analysis, if the virtual work principle is applied to the e-th element, and omitting body forces, then it is possible to write the following:

$$\int_{V_e} \delta\boldsymbol{\epsilon}^T \boldsymbol{\sigma} dV_e - \int_{A_e} \delta\boldsymbol{q}_e{}^T \boldsymbol{t} dA_e - \sum_k \delta(\boldsymbol{q}_e)_k{}^T \boldsymbol{f}_e = 0 \tag{7}$$

where the vector of the stress components is given as $\boldsymbol{\sigma} = \left[\sigma_x, \sigma_y, \sigma_z, \tau_{xy}, \tau_{xz}, \tau_{yz}\right]$, the surface tractions' vector is defined as $\boldsymbol{t} = \left[t_x, t_y, t_z\right]$ and $\boldsymbol{f}_k = \left[f_x, f_y, f_z\right]$ denotes the concentrated loads applied at node *k*. The nodal displacements for a generic k-th node are represented by the vector $(\boldsymbol{q}_e)_k = [u_k, v_k, w_k]$.

After some mathematical manipulation, one can achieve the following equilibrium equations for the e-th element:

$$\left(\int_{V_e} \boldsymbol{B}^T \boldsymbol{Q} \boldsymbol{B} dV_e\right) \boldsymbol{q}_e = \int_{A_e} \boldsymbol{N}^T \boldsymbol{t} dA_e - \sum_k \delta(\boldsymbol{q}_e)_k{}^T \boldsymbol{f}_k \tag{8}$$

$$\boldsymbol{K}_e \boldsymbol{q}_e = \boldsymbol{f}_e \tag{9}$$

The elastic coefficients matrix $\boldsymbol{Q}$ for the considered FGM distribution law given in Eq 5 follow the definitions presented in Reddy [39], with the particularity of being dependent on the thickness coordinate. The $\boldsymbol{B}$ matrix relates the strains with the displacements, and the $\boldsymbol{N}$ vector contains the interpolating Lagrange linear functions adopted to describe both the geometry of the domain and the displacements within the element. The element stiffness matrix, generalized displacements vector, and generalized forces vector are represented by $\mathbf{K}_e$, $\mathbf{q}_e$ and $\mathbf{f}_e$, respectively.

Extending these equilibrium equations to the whole discretized domain, and after applying the boundary conditions, the primary variables of the problem (i.e., the nodal displacements) are achieved. For the implementation of these equations, an 8-node hexahedron element (i.e., a trilinear element) was used, as depicted in Figure 3.

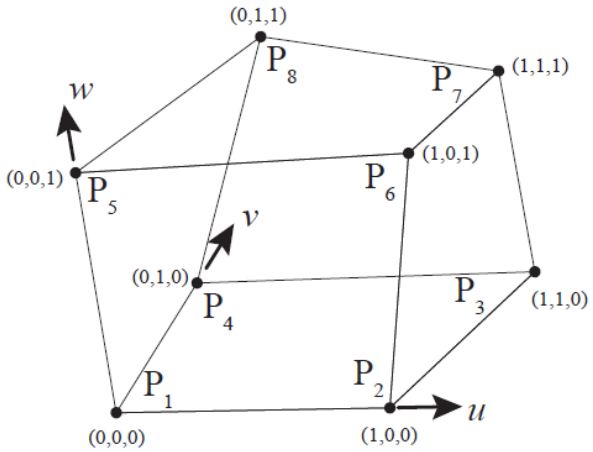


**Figure 3.** Generic 8-node hexahedron finite element and its local coordinate system.

Further details regarding the development and implementation of the model can be consulted in Carvalho [40].

## 3. Results and discussion

To study the performance of the proposed model, some verification studies were completed before performing a set of parametric cases.

### *3.1. Verification cases*

Static analyses were performed to a set of three rectangular, isotropic, homogeneous beams. The maximum transverse deflection and the normal stress at the corresponding location were used to verify the suitability of the model. The verification was made using the numerical solution based on the first-order shear deformation theory used by the SolidWorks software [41] for the thick beam and the Euler-Bernoulli theory used by the Ftool software [42] for the thinner beams as references.

The characteristics of the beams used in the analyses are presented in Table 2. The acronym (C) stands for clamped, meaning that all the nodal degrees of freedom at a specific extremity of the beam are constrained; the acronym (MS) stands for a moving support boundary condition, meaning that the corresponding extremity nodal displacements along the y and z directions are constrained. A uniformly distributed force is applied on the top surface of the beam.

**Table 2.** Characteristics of the beam.

| Beam ID | Dimensions L × w × h (mm) | Aspect ratio L/h | Elastic constants E (GPa), ν | Boundary conditions | Load (kPa) |
|---|---|---|---|---|---|
| 1 | 2000 × 20 × 20 | 100 | 200, 0.3 | C-C | –100 |
| 2 | 2000 × 20 × 20 | 100 | 200, 0.3 | C-MS | –100 |
| 3 | 200 × 20 × 20 | 10 | 200, 0.3 | C-C | –100 |

After performing the static analyses, the maximum displacements obtained for the beams are presented in Table 3, where *Nx* stands for the number of elements along the beam length and *NDoF* is the corresponding number for the degrees of freedom. The reference solution is presented in the last column. The deviations of the present model results to the reference are presented within parentheses and are determined as follows:

$$deviation = \frac{present - reference}{reference} 100\% \tag{10}$$

As the number of elements along the beam length increases, Table 3 shows a smaller deviation of the maximum transverse displacement in relation to the reference solution. The convergence for the thin beams requires a greater number of elements when compared to the moderately thick beam; however, for the moderately thick beam, a good agreement is obtained for a less refined domain. Moreover, it is possible to observe a beneficial agreement obtained for the normal longitudinal stress at the maximum deflection point for the three beams considered within the verification cases.

**Table 3.** Convergence summarized results and maximum displacements for the verification cases.

| Beam | Nx | 20 | 100 | 200 | 300 | 400 | 500 | Ref. | Ref. |
|---|---|---|---|---|---|---|---|---|---|
| ID | NDoF | 1134 | 5454 | 10854 | 28896 | 60150 | 108216 | [40] | [41] |
| 1 | w × $10^{-2}$ (m) | 0.293 | 2.19 | 2.75 | 2.94 | 3.02 | 3.06 | 3.13 | |
| | deviation (%) | –90.64 | –30.03 | –12.14 | –6.07 | –3.51 | –2.24 | | |
| | $\sigma_x$ (MPa) | | | | | | 249 | 250 | |
| 2 | w × $10^{-2}$ (m) | 0.607 | 4.56 | 5.72 | 6.13 | 6.28 | 6.36 | 6.50 | |
| | deviation (%) | –90.66 | –29.85 | –12.00 | –5.69 | –3.38 | –2.15 | | |
| | $\sigma_x$ (MPa) | | | | | | 421 | 422 | |
| 3 | w × $10^{-2}$ (m) | 2.98 | 3.44 | 3.46 | | | | | 3.47 |
| | deviation (%) | –14.12 | –0.86 | –0.29 | | | | | |
| | $\sigma_x$ (MPa) | | | 2.50 | | | | | 2.50 |

Thus, these results show that the model is suitable for the purpose of the present work.

### *3.2. Convergence analyses*

A set of studies were performed using I-shaped cross-section beams. The beam configuration used was a W150x100x24.0 beam and the ratio of the L/h varied between case studies. Additionally, in terms of boundary conditions, two cases were considered, namely a clamped-clamped (CC) boundary condition and a clamped-moving support (C-MS) boundary condition.

A convergence analysis was performed in relation to the maximum deflection parameter for different aspect ratios of $L/h = 10$ and $L/h = 2$.

The results are presented in Table 4, where *Nx* is the number of elements along the beam length, *NDoF* is the corresponding number of degrees of freedom, *Max W C-C* is the maximum deflection of the beam for the clamped-clamped boundary condition, and *Max W C-MS* is the maximum deflection of the beam for the clamped-moving support boundary condition.

For both boundary condition cases, the results for the moderately thick beam ($L/h = 10$) show a convergence for 200 elements along the length of the beam. Similarly, another convergence analysis

was performed to the thicker I-shaped cross-section beam ($L/h$ = 2) while considering the same boundary cases. The results for the maximum deflection are presented in Table 5 and, in this instance, the convergence is verified for fewer elements, specifically for 140 elements along the length of the beam.

**Table 4.** Convergence analysis of the I-shaped cross-section beam with L/h = 10 for both boundary cases.

| NX | NDoF | Max w C-C (mm) | Relative variation C-C (%) | Max w C-MS (mm) | Relative variation C-MS (%) |
|---|---|---|---|---|---|
| 20 | 7560 | 9.93E-05 | | 1.73E-04 | |
| 40 | 14760 | 1.06E-04 | 6.30 | 1.82E-04 | 5.18 |
| 60 | 26352 | 1.07E-04 | 1.63 | 1.84E-04 | 1.35 |
| 80 | 44712 | 1.09E-04 | 1.62 | 1.86E-04 | 1.03 |
| 100 | 65448 | 1.10E-04 | 0.48 | 1.87E-04 | 0.33 |
| 120 | 90024 | 1.10E-04 | 0.68 | 1.87E-04 | 0.43 |
| 140 | 118440 | 1.11E-04 | 0.19 | 1.88E-04 | 0.13 |
| 160 | 154560 | 1.11E-04 | 0.42 | 1.88E-04 | 0.27 |
| 180 | 191136 | 1.11E-04 | 0.28 | 1.89E-04 | 0.18 |
| 200 | 231552 | 1.11E-04 | 0.07 | 1.89E-04 | 0.04 |
| 220 | 286416 | 1.12E-04 | 0.20 | 1.89E-04 | 0.13 |
| 240 | 329688 | 1.12E-04 | 0.13 | 1.89E-04 | 0.08 |

**Table 5.** Convergence analysis of the I-shaped cross-section beam with L/h = 2 for both boundary cases.

| NX | NDoF | Max w C-C (mm) | Relative variation C-C (%) | Max w C-MS (mm) | Relative variation C-MS (%) |
|---|---|---|---|---|---|
| 20 | 13608 | 4.36E-06 | | 4.69E-06 | |
| 40 | 47232 | 5.37E-06 | 22.98 | 5.71E-06 | 21.66 |
| 60 | 103944 | 5.72E-06 | 6.68 | 6.07E-06 | 6.37 |
| 80 | 233280 | 5.91E-06 | 3.25 | 6.26E-06 | 3.13 |
| 100 | 432684 | 5.98E-06 | 1.25 | 6.33E-06 | 1.15 |
| 120 | 684618 | 6.06E-06 | 1.35 | 6.42E-06 | 1.43 |
| 140 | 1145484 | 6.10E-06 | 0.60 | 6.45E-06 | 0.46 |
| 160 | 1692432 | 6.16E-06 | 0.97 | 6.53E-06 | 1.17 |
| 180 | 2363136 | 6.13E-06 | –0.42 | 6.49E-06 | –0.64 |

### *3.3. Static behavior of the beams*

The present subsection presents the results obtained from the static analyses performed while considering the moderately thick and the thick beams under different boundary conditions and in any case submitted to a uniformly distributed load of 100 kPa. Because the flanges are very thin, the flanges are deemed to have a constant material distribution, and the parameters used in the volume fraction law for these case studies are presented in Table 6. The case studies presented in this subsection consider the material distribution shown in Figure 2, meaning that the main material in the web is steel and the flanges have a constant material distribution of alumina.

**Table 6.** Volume fraction law parameters.

| $z_{min}$ (%) | $z_{max}$ (%) | $z_{cutA}$ (%) | $z_{cutB}$ (%) | $C_1$ (%) | $C_{2A}$ | $C_{2B}$ |
|---|---|---|---|---|---|---|
| 6.44 | 93.56 | 45 | 55 | 0 | 10 | 10 |

The results are organized per boundary conditions, and, within each case, the transverse deflections and the stress distributions are analyzed.

#### 3.3.1. C-C boundary conditions

The static behavior of clamped-clamped FGM beams was analyzed and the results are presented in Tables Table **7** and Table 8. For a better quantitative illustration of the deflections' profiles along the length, three intermediate positions along the length of the beam were considered besides the extremities. As expected, at these latter locations, the transverse displacements were zero and the stress values suffered from the influence of the boundary conditions.

From Table 7, it can be observed that the maximum transverse deflection of the beams occurs in the middle of the beam and is greater for the moderately thick beam ($L/H$ = 10), as expected. Regarding the normal stresses, $\sigma_x$ is higher for this beam, with the highest values occurring in the bottom surface of the cross-section at the middle of the beam. As for $\sigma_y$, the highest stress values occur in the middle of the section but in different locations along the length of the beams. For the moderately thick beam, $\sigma_y$ occurs in the L/4 location of the beam; in the thick beam, $\sigma_y$ occurs in the middle of the beam. Additionally, normal stress $\sigma_z$ has the highest values in compression and occurs in different locations along both beams. For the moderately thick beam, $\sigma_z$ occurs at the bottom of the section at the 3L/4 location; in the thick beam, $\sigma_z$ occurs at the bottom of the section at the beam's mid-span. Considering the shear stresses, only $\tau_{xz}$ presents significant values. These are considerably higher for the moderately thick beam and have a similar value for the tension and the compression. The highest values occur in the same locations for both beams; the highest compression occurs in the bottom of the section in the L/4 location along the length, and the highest tension occurs in the bottom of the section in the 3L/4 location along the length of the beam.

**Table 7.** Deformation and normal stresses in the I-shaped cross-section beams with different aspect ratios for C-C boundary conditions.

| Location on the length | Location on the section | w (m) | | $\sigma_x$ (Pa) | | $\sigma_y$ (Pa) | | $\sigma_z$ (Pa) | |
|---|---|---|---|---|---|---|---|---|---|
| | | L/h = 10 | L/h = 2 | L/h = 10 | L/h = 2 | L/h = 10 | L/h = 2 | L/h = 10 | L/h = 2 |
| 0 | 0 | 0 | 0 | –1.85E+07 | –2.38E+06 | –7.91E+06 | –1.02E+06 | –7.91E+06 | –1.02E+06 |
| | H/2 | 0 | 0 | 1.93E+07 | 3.44E+06 | 8.25E+06 | 1.47E+06 | 8.25E+06 | 1.47E+06 |
| | H | 0 | 0 | –4.27E+05 | –6.32E+05 | –1.83E+05 | –2.71E+05 | –1.83E+05 | –2.71E+05 |
| L/4 | 0 | –4.67235E-05 | –8.33E-07 | 1.05E+06 | 1.95E+05 | –2.81E+04 | 9.72E+04 | 1.18E+04 | 6.22E+03 |
| | H/2 | –4.72E-05 | –1.23E-06 | –1.47E+04 | 5.11E+05 | 3.15E+06 | 2.64E+06 | 3.06E+05 | 3.06E+04 |
| | H | –4.69E-05 | –9.43E-07 | –5.12E+05 | –2.55E+05 | –2.76E+01 | –7.61E-02 | –1.55E+06 | –1.24E+06 |
| L/2 | 0 | –7.14E-05 | –1.21E-06 | 3.72E+06 | 3.16E+05 | –2.60E+04 | –6.63E+03 | 2.29E+04 | 4.09E+03 |
| | H/2 | –7.18E-05 | –1.68E-06 | –2.69E+06 | 6.46E+05 | 3.14E+06 | 3.21E+06 | 2.95E+05 | 4.94E+04 |
| | H | –7.17E-05 | –1.34E-06 | –7.71E+05 | –2.31E+05 | –2.79E+01 | –2.63E-02 | –1.55E+06 | –1.56E+06 |
| 3L/4 | 0 | –4.67E-05 | –8.33E-07 | 1.05E+06 | 1.95E+05 | –2.81E+04 | 9.72E+04 | 1.18E+04 | 6.22E+03 |
| | H/2 | –4.71E-05 | –1.23E-06 | –1.44E+04 | 5.11E+05 | 3.15E+06 | 2.64E+06 | 3.06E+05 | 3.06E+04 |
| | H | –4.69E-05 | –9.43E-07 | –5.12E+05 | –2.55E+05 | –2.76E+01 | –7.62E-02 | –1.55E+06 | –1.24E+06 |
| L | 0 | 0 | 0 | –1.85E+07 | –2.38E+06 | –7.91E+06 | –1.02E+06 | –7.91E+06 | –1.02E+06 |
| | H/2 | 0 | 0 | 1.92E+07 | 3.44E+06 | 8.23E+06 | 1.47E+06 | 8.23E+06 | 1.47E+06 |
| | H | 0 | 0 | –4.21E+05 | –6.32E+05 | –1.81E+05 | –2.71E+05 | –1.81E+05 | –2.71E+05 |

**Table 8.** Shear stresses in the I-shaped cross-section beams with different aspect ratios for C-C boundary conditions.

| Location on the length | Location on the section | $\tau_{xy}$ (Pa) | | $\tau_{yz}$ (Pa) | | $\tau_{yz}$ (Pa) | |
|---|---|---|---|---|---|---|---|
| | | L/h = 10 | L/h = 2 | L/h = 10 | L/h = 2 | L/h = 10 | L/h = 2 |
| 0 | 0 | –4.58E-01 | 8.76E+01 | –4.35E+06 | –5.99E+05 | –4.18E-10 | –7.92E-13 |
| | H/2 | 1.38E+00 | 2.88E+02 | –4.55E+06 | –8.52E+05 | 6.99E-10 | 2.76E-10 |
| | H | –2.04E+00 | –1.63E+02 | –1.08E+07 | –1.95E+06 | 6.29E-09 | 4.15E-10 |
| L/4 | 0 | –3.10E+01 | 3.48E+02 | –5.85E+04 | –5.10E+03 | –2.90E-01 | 8.57E+00 |
| | H/2 | 4.59E+01 | 2.94E+03 | –5.85E+04 | –2.34E+02 | 1.66E+00 | 2.13E+02 |
| | H | –2.72E-01 | –9.52E+01 | –8.17E+06 | –1.59E+06 | –5.88E-01 | –1.30E+02 |
| L/2 | 0 | 2.26E+01 | 6.56E+00 | 1.90E+00 | 8.19E-01 | –8.17E+00 | 3.25E+01 |
| | H/2 | 8.68E+01 | 2.10E+03 | 1.90E+00 | 2.79E+01 | 5.62E+00 | 9.47E+01 |
| | H | –1.94E+00 | –1.08E+01 | 2.65E+02 | 3.55E+02 | 1.15E+00 | –3.47E+02 |
| 3L/4 | 0 | 2.71E+02 | –3.51E+02 | 5.85E+04 | 5.10E+03 | –1.97E+01 | 1.01E+01 |
| | H/2 | 4.88E+02 | –3.17E+03 | 5.85E+04 | 2.35E+02 | 7.49E+01 | 2.15E+02 |
| | H | –1.43E+01 | 1.04E+02 | 8.17E+06 | 1.59E+06 | –2.20E+01 | –1.46E+02 |
| L | 0 | –5.83E+01 | –8.87E+01 | 4.35E+06 | 5.99E+05 | –1.88E-07 | 1.14E-08 |
| | H/2 | –7.21E+03 | –3.27E+02 | 4.54E+06 | 8.52E+05 | –1.94E-07 | 1.64E-08 |
| | H | 5.57E+03 | 1.81E+02 | 1.08E+07 | 1.95E+06 | –3.93E-07 | 4.16E-08 |

To better illustrate these results, Figure 4a shows the displacement profiles for both beams, where the solid lines correspond to the results of the L/h = 2 beam and the dotted lines correspond to the results of the L/h = 10 beam. The horizontal axis of the graphs denotes the relative length coordinates of the beams (x/L) so that the results may be compared among the beams of varying lengths. Three lines are presented for each case, which correspond to the positions through the cross-section of the beam: in the bottom surface (z = 0 m), in the middle surface (z = 0.08 m), and in the top surface (z = 0.16 m).

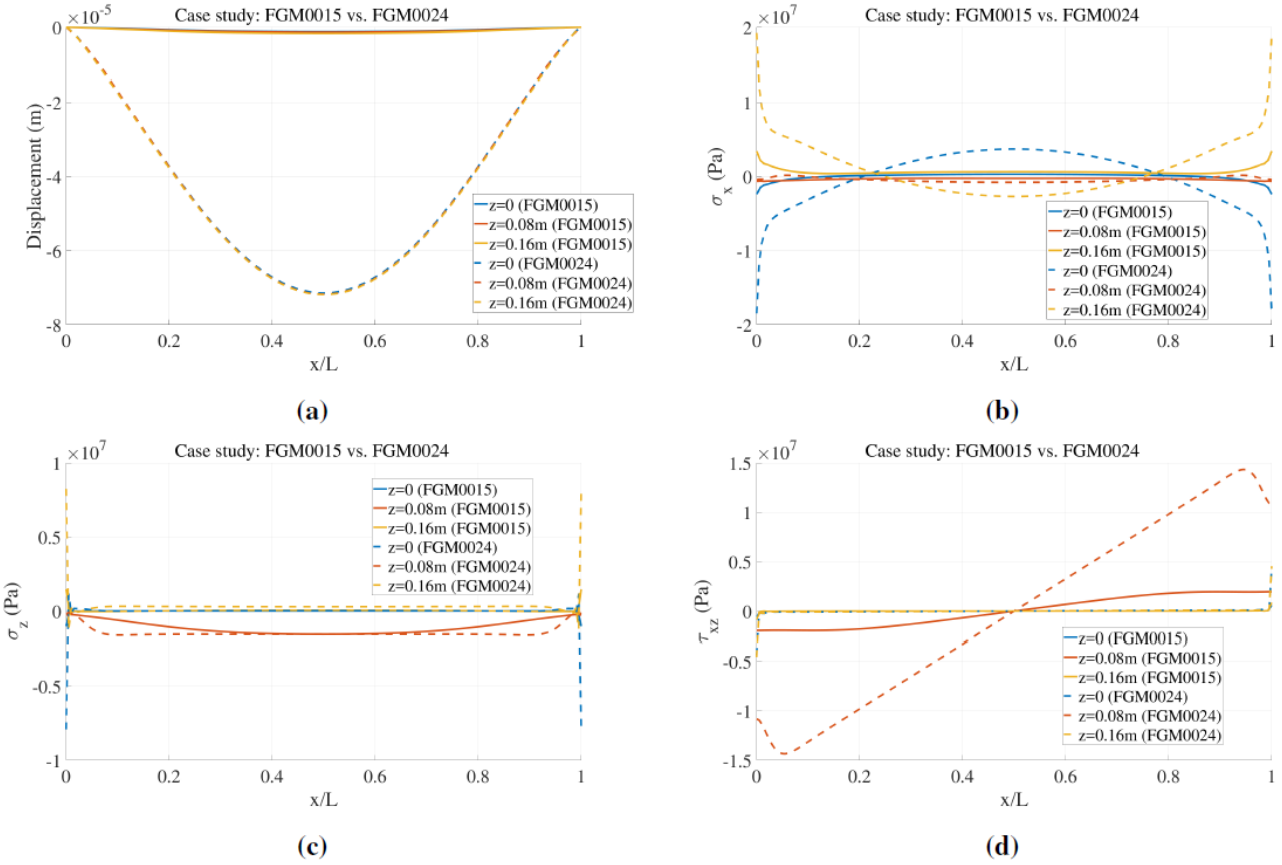


**Figure 4.** Stresses along the length of the beam for I-shaped cross-section beam with C-C boundary conditions with L/h = 2 (solid lines) and L/h = 10 (dotted lines) (a) Transverse displacement (b) Normal stress $\sigma_x$ (c) Normal stress $\sigma_z$ (d) Shear stress $\tau_{xz}$.

Regarding the normal stresses along the length of the beam, Figure 4b presents $\sigma_x$ along that direction and, for both aspect ratios, this stress presents a higher variation in the flanges, as well as at the center of the cross-section. This distribution profile is influenced by the material distribution through the cross-section (Figure 2).

It is interesting to note that both beams present the same behavior; however, for the thicker beam, the stress on the top of the section is always higher than the stress on the bottom of the section, and the stress in the middle of the section is lower than the other two. In the thinner beam, the stress in the middle of the section is constant and close to zero, and the stresses in the top and bottom of the section show an almost symmetrical behavior, changing from tension to compression, or vice-versa. If $\sigma_z$ is considered (Figure 4c), a non-symmetrical distribution was evident through the height of the beam, as was expected.

As highlighted in Figure 4d, the shear stress $\tau_{xz}$ along the length of the beam shows a symmetrical behavior with respect to the mid-height point of the cross-section, with a zero value in the middle length of the beam.

Analyzing the stresses along the section, Figure 5 presents the stress $\sigma_x$ for three positions along the length of the beam. In Figure 6, the stress $\sigma_z$ in the cross-section is presented for three positions along the length of the beam. The behavior of this stress is similar for both beams, with higher stresses on the flanges and a considerable compression below the top flange. Additionally, the thicker beam presents higher stresses in the equivalent locations along the length of the beam.

As noticed from Table 8, the shear stress $\tau_{xz}$ along the length of the beams has a relevant distribution. As such, Figure 7 presents the profile in the cross-section for three positions along the length of the beam. The profiles for both beams are similar, showing that the web is subjected to more shear stress, and with higher values for the moderately thick beam.

These results are consistent with the expected trends associated with the higher and lower aspect ratios of the beams. It is also important to note that because the deformation is not completely symmetric along the cross-section, it contributes to the stress profiles of the beams. Additionally, the effect of the geometric variation of the I-shaped cross-section also influences the results.

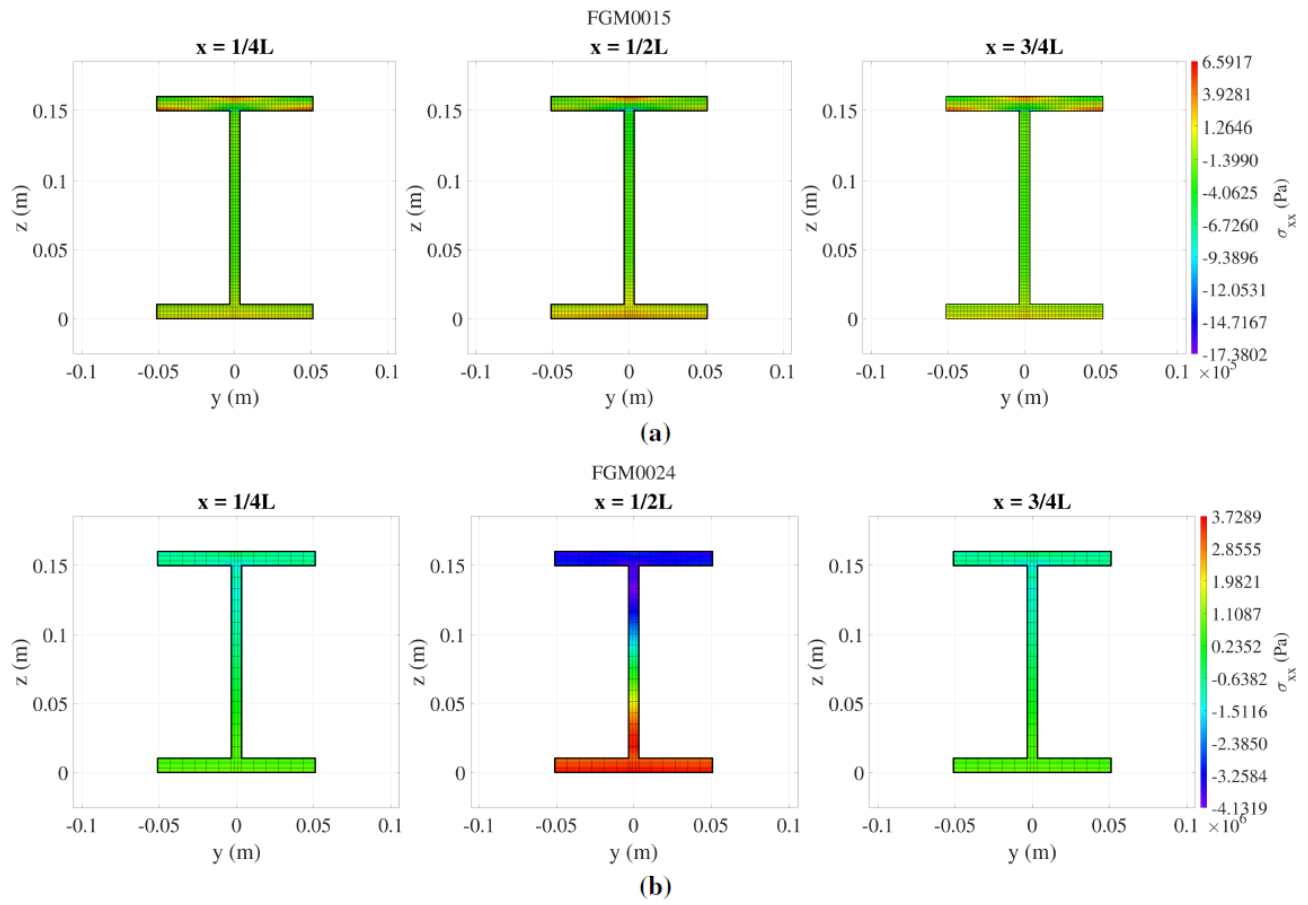


**Figure 5.** Normal stress $\sigma_x$ for I-shaped cross-section beam with C-C boundary conditions with (a) L/h = 2 (b) L/h = 10.

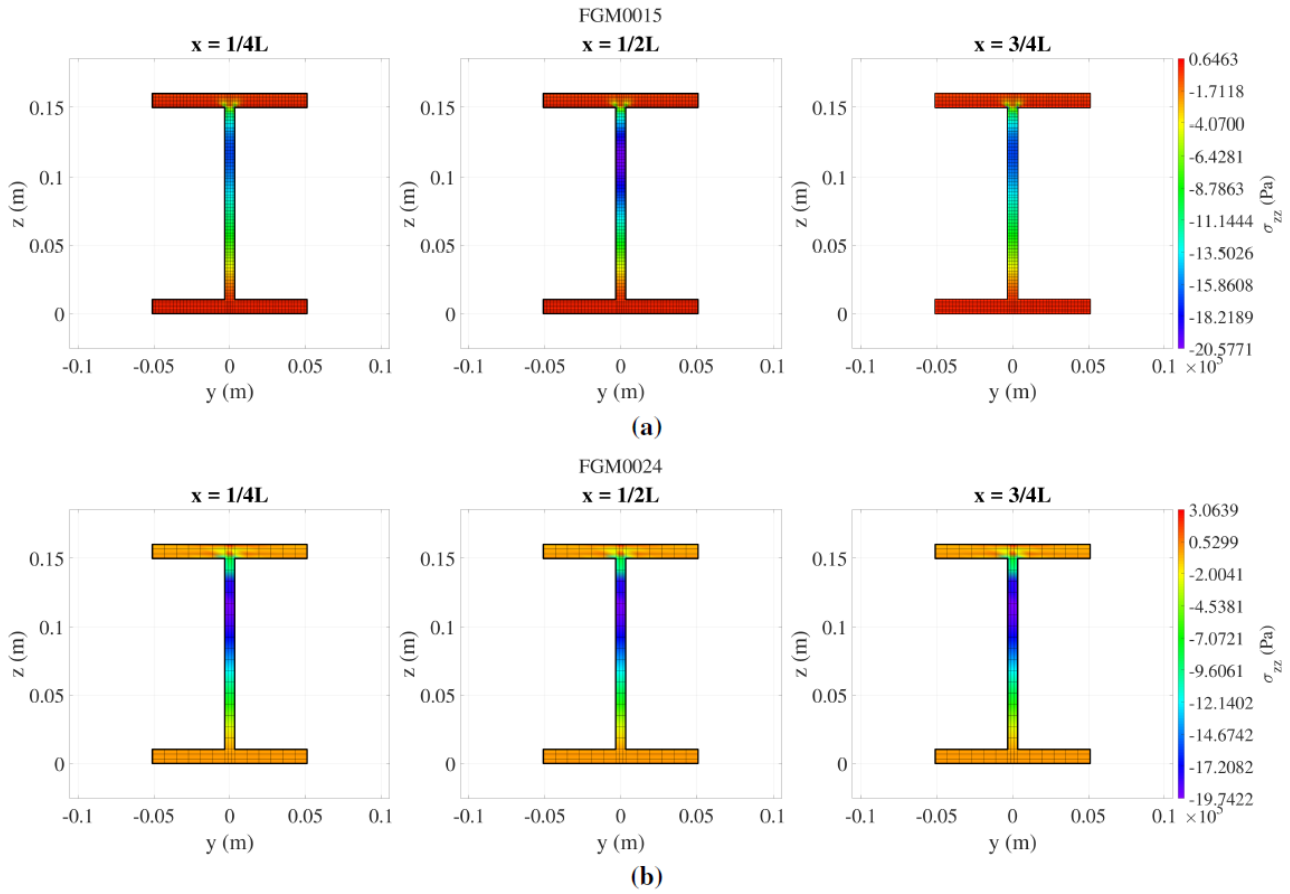


**Figure 6.** Normal stress $\sigma_z$ for I-shaped cross-section beam with C-C boundary conditions with (a) L/h = 2 (b) L/h = 10.

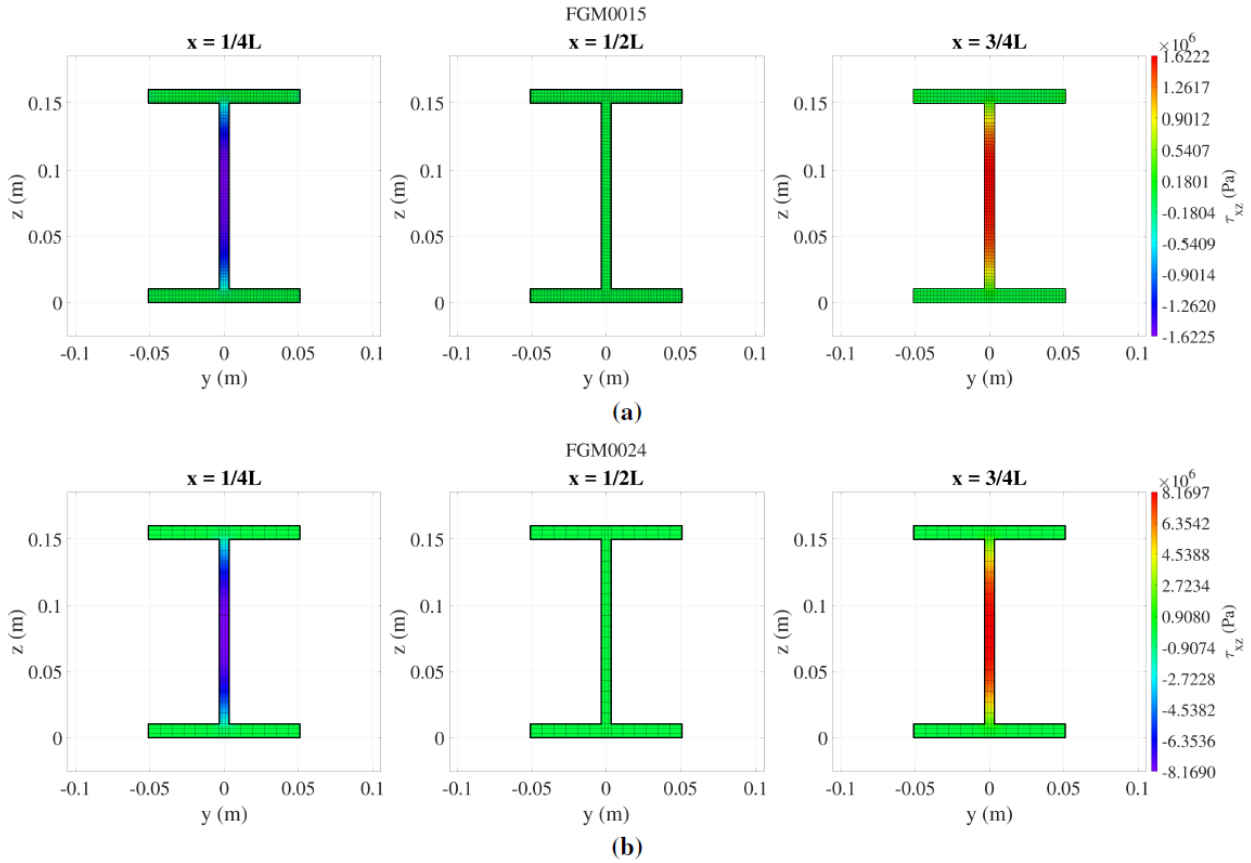


**Figure 7.** Shear stress $\tau_{xz}$ for I-shaped cross-section beam with C-C boundary conditions with (a) L/h = 2 (b) L/h = 10.

### 3.3.2. C-MS boundary conditions

In this case study, the two beams ($L/h$ = 10 and $L/h$ = 2) were analyzed while considering a clamped extremity and a moving support boundary condition on the other extremity. The same 100 kPa transverse, uniformly distributed load was applied.

Table 9 presents the results for the maximum transverse displacement and normal stresses, and Table 10 presents the results for the shear stress. The maximum deflection occurs in similar sections along the length of the beam, with higher values for the thinner beam, as expected. Moreover, regarding the cross section for this beam, a higher transverse displacement occurs on the top of the section, whereas on the thick beam, it occurs in the middle of the section. From the results for the longitudinal normal stresses, $\sigma_x$ is considerably higher on the moderately thick beam, with the maximum values occurring at the mid-length and in the bottom of the section. Considering $\sigma_y$, the maximum values occur in the middle of the section at L/4 for the thinner beam and in the middle of the section at L/2 for the thick beam. In this case, the thicker beam presents higher values. The same observations may be made for $\sigma_z$.

As for the shear stress, Table 10 shows that $\tau_{xz}$ exhibits relevant values in the module (i.e., 12 MPa) occurring at the bottom of the section at L/4 for the moderately thick beam and 1.9 MPa in the same location on the thick beam. Moreover, at the bottom of the section at 3L/4, there was a stress value of 4.3 MPa for the moderately thick beam and a stress value of 1.3 MPa for the thick beam. In comparison, the other shear stresses were not so relevant.

**Table 9.** Deformation and normal stresses in the I-shape beams with different aspect ratios for C-MS boundary conditions.

| Location on the length | Location on the section | w (m) | | $\sigma_x$ (Pa) | | $\sigma_y$ (Pa) | | $\sigma_z$ （Pa） | |
|---|---|---|---|---|---|---|---|---|---|
| | | L/h = 10 | L/h = 2 | L/h = 10 | L/h = 2 | L/h = 10 | L/h = 2 | L/h = 10 | L/h = 2 |
| 0 | 0 | 0 | 0 | –2.45E+07 | –2.48E+06 | –1.05E+07 | –1.06E+06 | –1.05E+07 | –1.06E+06 |
| | H/2 | 0 | 0 | 2.54E+07 | 3.68E+06 | 1.09E+07 | 1.58E+06 | 1.09E+07 | 1.58E+06 |
| | H | 0 | 0 | –1.55E+05 | –5.67E+05 | –6.65E+04 | –2.43E+05 | –6.65E+04 | –2.43E+05 |
| L/4 | 0 | –6.56E-05 | –9.53E-07 | 6.78E+05 | 3.73E+05 | –2.85E+04 | 1.12E+05 | 1.00E+04 | 6.93E+03 |
| | H/2 | –6.61E-05 | –1.36E-06 | 4.50E+05 | 4.08E+05 | 3.15E+06 | 2.63E+06 | 3.08E+05 | 2.98E+04 |
| | H | –6.58E-05 | –1.08E-06 | –3.84E+05 | –1.86E+05 | –2.75E+01 | –7.67E-02 | –1.55E+06 | –1.24E+06 |
| L/2 | 0 | –1.13E-04 | –1.41E-06 | 5.86E+06 | 5.39E+05 | –2.44E+04 | –1.06E+04 | 3.16E+04 | 4.42E+03 |
| | H/2 | –1.14E-04 | –1.90E-06 | –4.74E+06 | 5.16E+05 | 3.14E+06 | 3.22E+06 | 2.87E+05 | 4.98E+04 |
| | H | –1.14E-04 | –1.57E-06 | –8.88E+05 | –1.37E+05 | –2.81E+01 | –2.02E-02 | –1.55E+06 | –1.61E+06 |
| 3L/4 | 0 | –9.10E-05 | –1.03E-06 | 5.71E+06 | 4.29E+05 | –2.46E+04 | –5.02E+03 | 3.09E+04 | 3.73E+03 |
| | H/2 | –9.15E-05 | –1.52E-06 | –4.58E+06 | 4.34E+05 | 3.14E+06 | 3.02E+06 | 2.87E+05 | 4.27E+04 |
| | H | –9.15E-05 | –1.18E-06 | –8.73E+05 | 6.91E+04 | –2.81E+01 | –5.55E-02 | –1.55E+06 | –1.50E+06 |
| L | 0 | 0 | 0 | 6.82E+04 | 5.71E+03 | 2.92E+04 | 2.45E+03 | 2.92E+04 | 2.45E+03 |
| | H/2 | 0 | 0 | –1.25E+05 | –3.43E+04 | –5.36E+04 | –1.47E+04 | –5.36E+04 | –1.47E+04 |
| | H | 0 | 0 | 3.52E+04 | 1.17E+04 | 1.51E+04 | 5.02E+03 | 1.51E+04 | 5.02E+03 |

**Table 10.** Shear stresses in the I-shaped cross-section beams with different aspect ratios for C-MS boundary conditions.

| Location on the length | Location on the section | $\tau_{xy}$ (Pa) | | $\tau_{yz}$ (Pa) | | $\tau_{yz}$ (Pa) | |
|---|---|---|---|---|---|---|---|
| | | L/h = 10 | L/h = 2 | L/h = 10 | L/h = 2 | L/h = 10 | L/h = 2 |
| 0 | 0 | –4.95E+00 | 8.83E+01 | –5.67E+06 | –6.26E+05 | 4.01E-10 | 6.23E-11 |
| | H/2 | 5.88E+00 | 3.24E+02 | –5.89E+06 | –9.13E+05 | 2.13E-09 | 2.83E-10 |
| | H | –3.87E+00 | –1.79E+02 | –1.33E+07 | –2.25E+06 | –5.60E-09 | 1.73E-10 |
| L/4 | 0 | –2.70E+02 | 4.02E+02 | –8.61E+04 | –6.26E+03 | 3.83E+00 | 8.32E+00 |
| | H/2 | 3.02E+02 | 3.14E+03 | –8.61E+04 | –1.38E+03 | 7.68E+00 | 2.14E+02 |
| | H | –4.02E-01 | –1.02E+02 | –1.20E+07 | –1.94E+06 | –4.97E+00 | –1.38E+02 |
| L/2 | 0 | –1.35E+02 | 5.10E+01 | –2.75E+04 | –1.05E+03 | –2.49E+01 | 3.47E+01 |
| | H/2 | 3.54E+02 | 2.34E+03 | –2.75E+04 | –1.04E+03 | 2.20E+00 | 1.02E+02 |
| | H | –3.65E+00 | –1.78E+01 | –3.84E+06 | –3.67E+05 | 9.83E+00 | –3.67E+02 |
| 3L/4 | 0 | 6.28E+02 | –3.48E+02 | 3.10E+04 | 5.37E+03 | –7.07E+01 | 2.04E+01 |
| | H/2 | 8.70E+02 | –3.03E+03 | 3.10E+04 | 4.36E+02 | 1.15E+02 | 2.48E+02 |
| | H | –2.77E+01 | 8.58E+01 | 4.32E+06 | 1.34E+06 | –1.60E+01 | –1.77E+02 |
| L | 0 | –1.79E+03 | –4.77E+02 | 8.75E+04 | 8.95E+03 | –8.54E-07 | 2.33E-08 |
| | H/2 | –3.82E+04 | –2.63E+03 | 6.02E+04 | 9.50E+03 | –8.60E-07 | 4.46E-08 |
| | H | 9.14E+02 | 5.25E+01 | 1.20E+07 | 2.48E+06 | –1.48E-06 | 5.37E-08 |

From Figure 8a, it can be observed that the maximum transverse displacement occurs slightly after the middle of the beam, toward the right-hand side, especially for the L/h = 10 beam (dotted lines), which is explained by the decreased restrictive boundary conditions at this extremity. The longitudinal normal stress $\sigma_x$ also accompanies this deviation to the right of the beam's mid-span, which is more clearly seen for the thinner beam. As for $\sigma_z$, both beams present a similar behavior. However, for the shear stress $\tau_{xz}$, although the behavior pattern is the same, there are higher values in the middle section for the moderately thick beam. It may also be seen that these stress distributions are not symmetrical on the length of the beams, which also implies the influence of differentiated restrictions introduced via the boundary conditions.

To allow for a more illustrative perception of the stress distributions through the section height of the beam, Figure 9 depicts those profiles for some situations.

The normal stress $\sigma_x$ presents a different behavior between the two beams ($L/h$ = 2 and $L/h$ = 10). Besides the different values that this stress assumes, the moderately thick beam for the L/4 section only shows tensile stresses through the thickness. Again, this is consistent with the effect introduced by the different boundary conditions.

Regarding $\sigma_z$, in Figure 10, there is a similar distribution on both beams but with higher values for the moderately thick beam. Additionally, it is visible that these higher values are sensed in web regions closer to the surface where the transverse load was applied.

As for the $\tau_{xz}$ distribution along the cross section of the beam, as shown in Figure 11, both beams present a similar behavior in the web, except for the case of the thick beam for the midspan coordinate. However, the moderately thick beam presents higher values of this shear stress in both flanges over the length of the beam.

Once again, these results show the influence of the material distribution along the transverse section of the beam, as well as the geometry influence on the stresses.

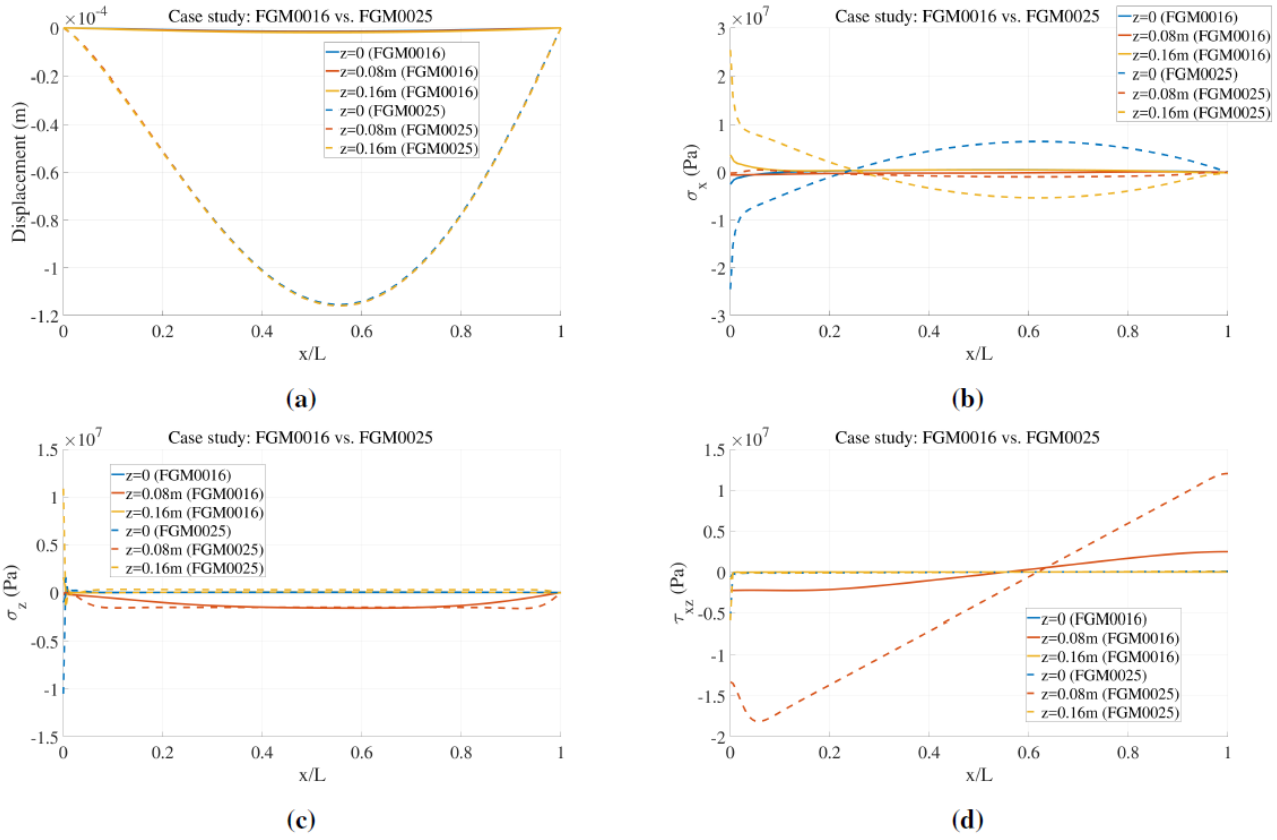


**Figure 8.** Results along the length of the beam for I-shaped cross-section beam with C-MS boundary conditions with L/h = 2 (solid lines) and L/h = 10 (dotted lines) (a) Deformation (b) Normal stress $\sigma_x$ (c) Normal stress $\sigma_z$ (d) Shear stress $\tau_{xz}$.

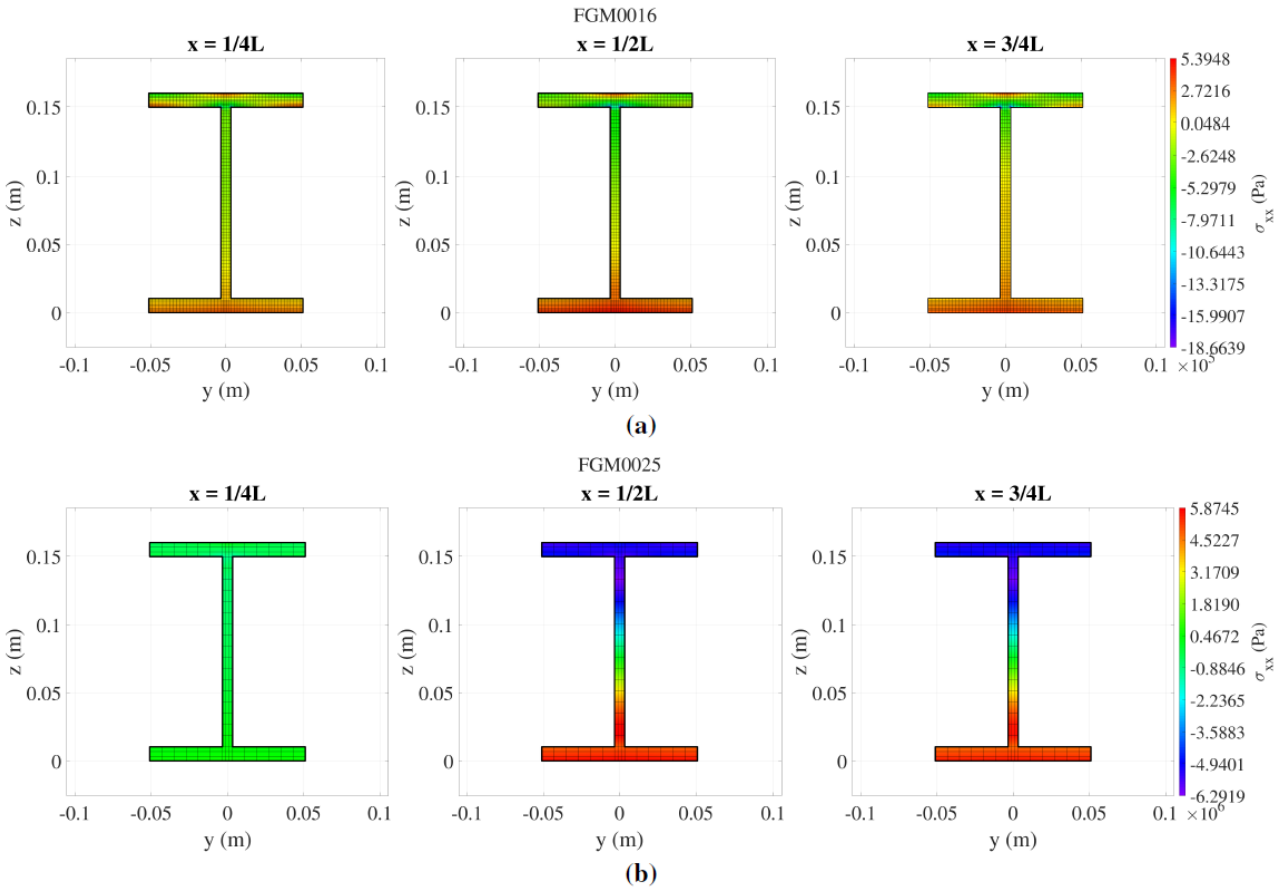


**Figure 9.** Normal stress $\sigma_x$ for I-shaped cross-section beam with C-MS boundary conditions with (a) L/h = 2 (b) L/h = 10.

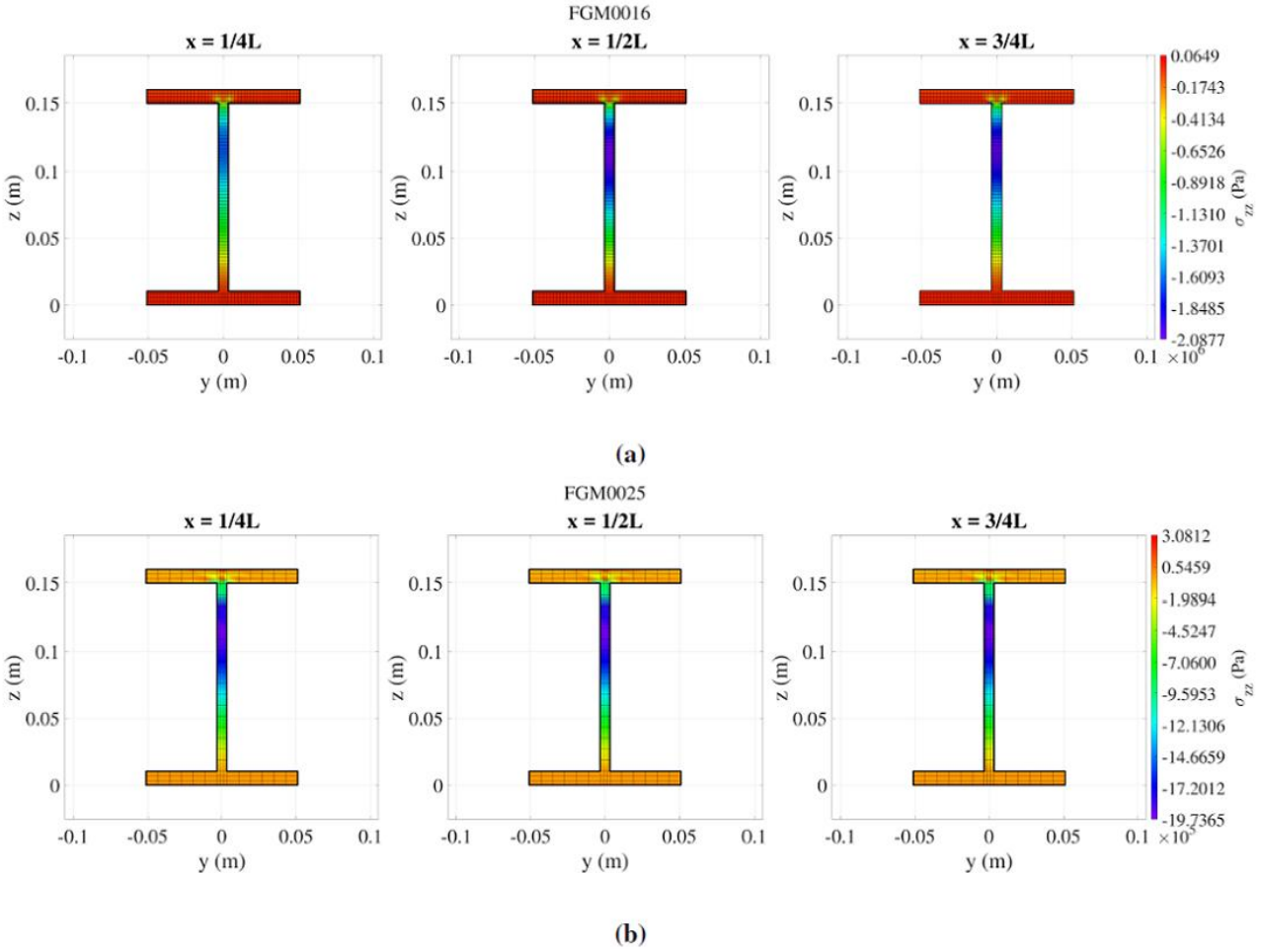


**Figure 10.** Normal stress $\sigma_z$ for I-shaped cross-section beam with C-MS boundary conditions with (a) L/h = 2 (b) L/h = 10.

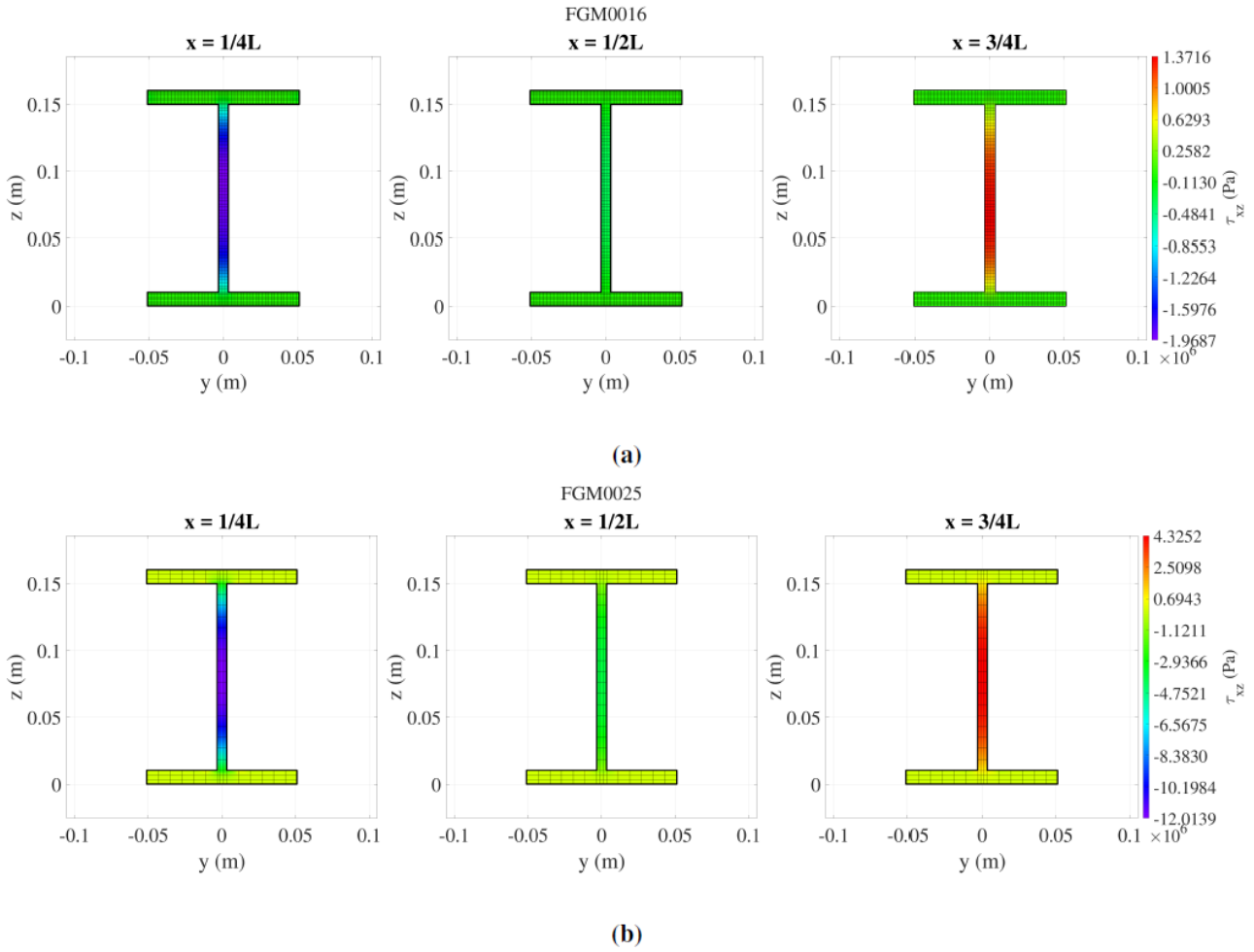


**Figure 11.** Shear stress $\tau_{xz}$ for I-shaped cross-section beam with C-MS boundary conditions with (a) L/h = 2 (b) L/h = 10.

### *3.4. Effect of volume fraction variation in the flanges*

The previous case studies considered a constant material distribution on the flanges due to their relatively thin character. Therefore, to illustrate the effect of the graded material distribution on the flanges, another case study is presented, where a beam with an aspect ratio L/h = 10 and C-C boundary conditions was subjected to a uniformly distributed load of 100 kPa. The volume fraction in this beam has the following parameters: $z_{min}$ = 0%, $z_{max}$ = 100%, $z_{cutA}$ = 50%, $z_{cutB}$ = 50%, $C_1$ = 0%, $C_{2A}$ = 10, and $C_{2B}$ = 10. As in the previous case studies, the main material on the web is material A, while in the flanges, it is material B. The gradation conforms with Eq 1.

Table 11 presents the deflection of the beam, as well as the resulting stresses along the length of the beam and along its cross-section.

**Table 11.** Deformation and stresses in an I-shaped cross-section beam with L/h = 10 for C-C boundary conditions considering varying material distribution on the flanges.

| Location on the length | Location on the section | w (m) | $\sigma_x$ (Pa) | $\sigma_y$ (Pa) | $\sigma_z$ (a) | $\tau_{xy}$ (Pa) | $\tau_{xz}$ (Pa) | $\tau_{yz}$ (Pa) |
|---|---|---|---|---|---|---|---|---|
| 0 | 0 | 0 | –2.01E+07 | –8.62E+06 | –8.62E+06 | 1.62E-07 | –4.77E+06 | –9.83E-10 |
| | H/2 | 0 | 2.09E+07 | 8.97E+06 | 8.97E+06 | 1.62E-06 | –4.98E+06 | 5.59E-10 |
| | H | 0 | –2.59E+05 | –1.11E+05 | –1.11E+05 | –4.49E-06 | –1.12E+07 | 3.77E-09 |
| L/4 | 0 | –5.09E-05 | 1.18E+06 | –3.20E+04 | 1.25E+04 | –1.98E-05 | –6.35E+04 | –2.69E-06 |
| | H/2 | –5.13E-05 | –2.52E+04 | 3.48E+06 | 3.51E+05 | 8.18E-06 | –6.35E+04 | –1.24E-06 |
| | H | –5.11E-05 | –5.31E+05 | –5.81E+01 | –1.55E+06 | 1.96E-07 | –8.16E+06 | –8.87E-06 |
| L/2 | 0 | –7.82E-05 | 4.22E+06 | –3.00E+04 | 2.46E+04 | –4.28E-06 | –5.49E-07 | 5.81E-06 |
| | H/2 | –7.86E-05 | –3.07E+06 | 3.48E+06 | 3.39E+05 | –2.58E-06 | –4.66E-07 | –3.96E-06 |
| | H | –7.85E-05 | –8.27E+05 | –5.78E+01 | –1.55E+06 | 1.02E-06 | 9.45E-06 | –3.06E-05 |
| 3L/4 | 0 | –5.09E-05 | 1.18E+06 | –3.20E+04 | 1.25E+04 | 2.01E-05 | 6.35E+04 | 6.71E-06 |
| | H/2 | –5.13E-05 | –2.52E+04 | 3.48E+06 | 3.51E+05 | –2.32E-05 | 6.35E+04 | 3.50E-06 |
| | H | –5.11E-05 | –5.31E+05 | –5.81E+01 | –1.55E+06 | 5.71E-07 | 8.16E+06 | –1.23E-05 |
| L | 0 | 0 | –2.01E+07 | –8.62E+06 | –8.62E+06 | 2.00E-06 | 4.77E+06 | –2.04E-07 |
| | H/2 | 0 | 2.09E+07 | 8.97E+06 | 8.97E+06 | –2.26E-06 | –4.98E+06 | –2.11E-07 |
| | H | 0 | –2.59E+05 | –1.11E+05 | –1.11E+05 | –3.29E-07 | 1.12E+07 | –4.14E-07 |

Comparing these results with the results presented in Tables 7 and 8 for the I-shaped cross-sectional beam with L/h = 10 and C-C boundary conditions, it can be said that the beam shows a slightly higher deformation along the cross-section when there is variation of the material distribution on the flanges. This is to be expected since the elasticity of the material in the flanges gradually decreases. The opposite behavior is expected if the materials' mixture was chosen to progress in the reverse direction. Additionally, the stresses are very similar, with no variation in the behavior of the two beams.

These conclusions may be confirmed by observing Figure 12, where the deformation and stress profiles along the beam are presented. No significant differences are observed in the beam that considers a variation in the material distribution on the flanges as compared to the beam that considers a uniform material distribution in the flanges.

Regarding the stress along the cross-sectional area, Figure 13 shows a similar behavior to the stress of the beam with a uniform material distribution in the flanges, as previously depicted in Figure 5b, 6b, and 7b. However, it is possible to observe that, by not limiting the material gradient distribution in the flanges, higher stresses are developed near the geometric variation between the flanges and the web due to this alteration in geometry.

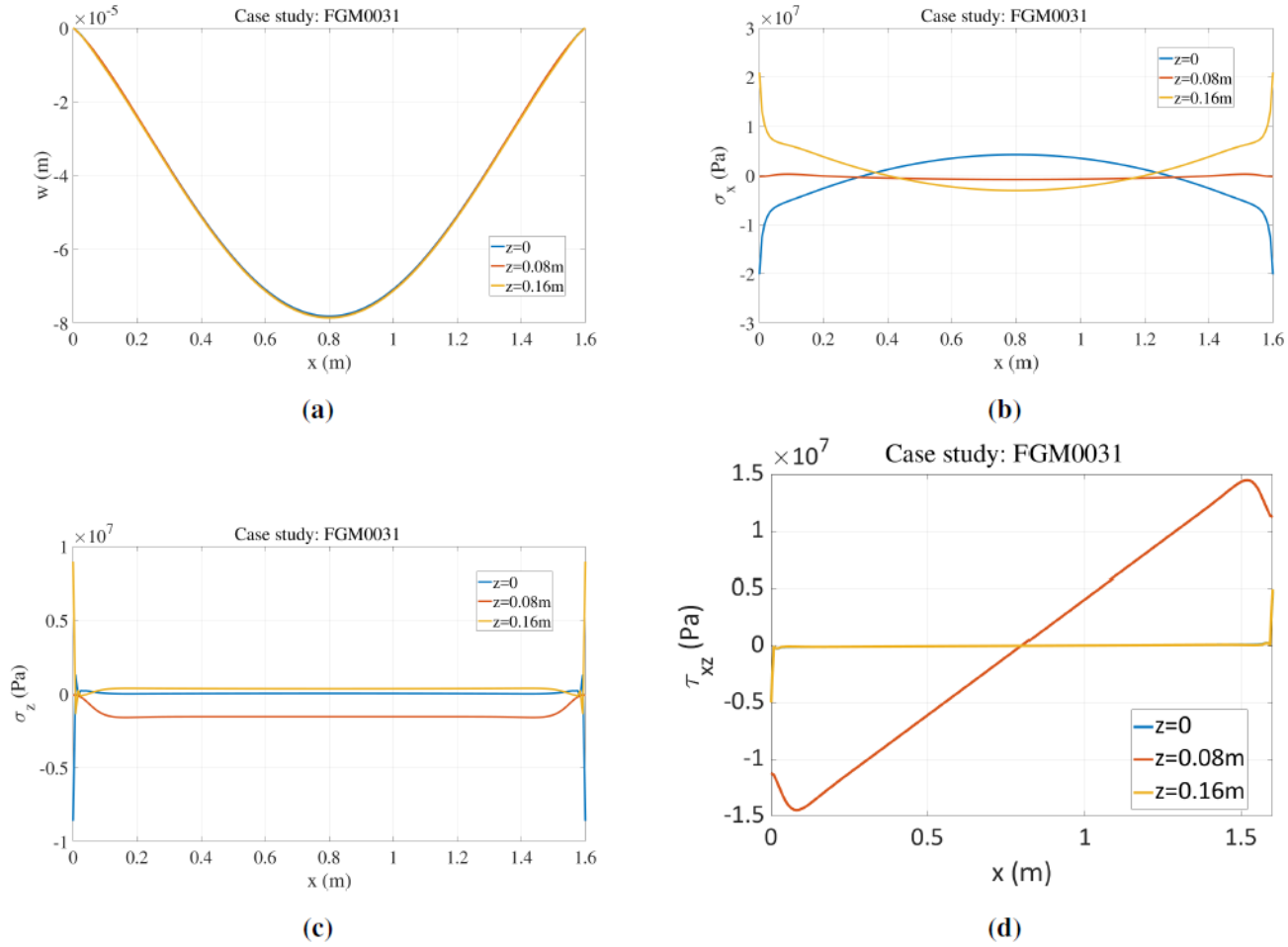


**Figure 12.** Results along the length of the beam for I-shaped cross-section beam with C-MS boundary conditions with L/h = 10 and varying material distribution in the flanges (a) Deformation (b) Normal stress $\sigma_x$ (c) Normal stress $\sigma_z$ (d) Shear stress $\tau_{xz}$.

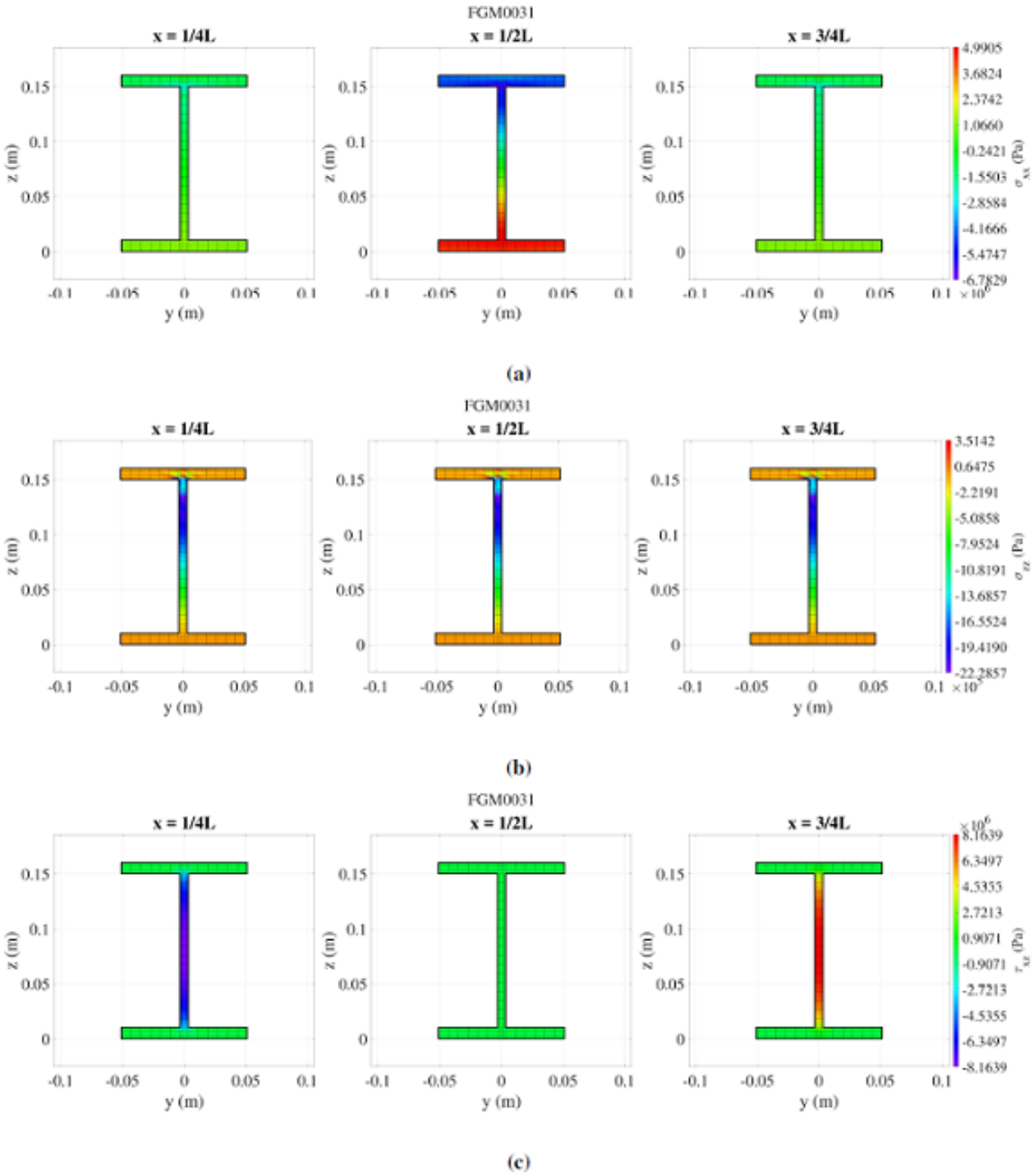


**Figure 13.** Stresses $\sigma_x$, $\sigma_z$ and $\tau_{xz}$ for I-shaped cross-section beam with C-C boundary conditions and L/h = 10, considering material distribution in the flanges.

## 4. Conclusions

The purpose of this study was to investigate the behavior of I-shaped cross-section beams made from functionally graded material under a uniformly distributed loading. To this purpose, an 8-node hexahedron solid finite element model was developed and implemented, which accounted for a

material mixture distribution through the thickness of the beam.

A set of verification studies were carried out to assess the performance of the model. The geometrical configuration of the beams used for the parametric study corresponded to a W150x100x24.0 beam. Two length-to-thickness ratios (L/h) were considered, namely a moderately thick beam (L/h = 10) and a thick beam (L/h = 2). Convergence analyses were performed to determine the most suitable discretization to adopt.

From the studies performed, it is feasible to conclude that the following:

- The FGM distribution affects the stress profile, and the values and location of maximum values through the beam's thickness accordingly;
- The boundary conditions influence the beam's deflected profile and, inherently, the maximum transverse displacement;
- There is a clear influence on the aspect ratio of the stress distribution through the cross-section, in particular on $\sigma_z$;
- Significant shear stress values, $\tau_{xz}$, appear in the beam's thickness, especially in the moderately thick beam.

This study shows the importance of investigating the influence of the use of functionally graded materials in beams with different cross-sections. There are several differences with respect to the behavior of rectangular-shaped cross-section beams, in particular, the appearance of transverse shear and normal stress profiles that should not be neglected.

## Acknowledgments

The authors acknowledge the support of FCT/MEC through Project IDMEC, LAETA UIDB/50022/2020. The authors also acknowledge the support of Project IPL/2022/VF_FGM_ISEL.

## Conflict of interest

M.A.R. Loja is an editorial board member/editor-in-chief for AIMS Materials Science and was not involved in the editorial review or the decision to publish this article. All authors declare that there are no competing interests.

## References

1. Koizumi M (1997) FGM activities in Japan. *Compos B Eng* 28: 1–4. https://doi.org/10.1016/S1359-8368(96)00016-9
2. Sayyad AS, Ghugal YM (2019) Modeling and analysis of functionally graded sandwich beams: a review. *Mech Adv Mater Struct* 26: 1776–1795. https://doi.org/10.1080/15376494.2018.1447178
3. Saleh B, Jiang J, Fathi R, et al. (2020) 30 years of functionally graded materials: An overview of manufacturing methods, applications and future challenges. *Compos B Eng* 201: 108376. https://doi.org/10.1016/j.compositesb.2020.108376
4. Garg A, Belarbi MO, Chalak H, et al. (2021) A review of the analysis of sandwich fgm structures. *Compos Struct* 258: 113427. https://doi.org/10.1016/j.compstruct.2020.113427

5. Parihar RS, Setti SG, Sahu RK (2018) Recent advances in the manufacturing processes of functionally graded materials: A review. *IEEE J Sel Top Quantum Electron* 25: 309–336. https://doi.org/10.1515/secm-2015-0395
6. Kanu NJ, Vates UK, Singh GK, et al. (2019) Fracture problems, vibration, buckling, and bending analyses of functionally graded materials: A state-of-the-art review including smart FGMS. *Part Sci Technol* 37: 583–608. https://doi.org/10.1080/02726351.2017.1410265
7. Banks-Sills L, Eliasi R, Berlin Y (2002) Modeling of functionally graded materials in dynamic analyses. *Compos B Eng* 33: 7–15. https://doi.org/10.1016/S1359-8368(01)00057-9
8. Kasem MM, Maalawi KY (2021) Multiobjective optimization of functionally graded material columns. *2021 3rd Novel Intelligent and Leading Emerging Sciences Conference (NILES)* 323–326. https://doi.org/10.1109/NILES53778.2021.9600498
9. Dastjerdi FB, Jabbari M (2022) Analytical analysis for non-homogeneous two-layer functionally graded material. *Nonlinear Eng* 11: 598–608. https://doi.org/10.1515/nleng-2022-0258
10. He D, Wang Q, Zhong R, et al. (2023) Vibration analysis of functionally graded material (FGM) double layered floating raft structure by the spectro-geometric method. *Struct* 48: 533–550. https://doi.org/10.1016/j.istruc.2022.11.111
11. Nguyen TT, Kim NI, Lee J (2016) Analysis of thin-walled open-section beams with functionally graded materials. *Compos Struct* 138: 75–83. https://doi.org/10.1016/j.compstruct.2015.11.052
12. Loja MA, Barbosa JI (2020) In-plane functionally graded plates: A study on the free vibration and dynamic instability behaviours. *Compos Struct* 237: 4. https://doi.org/10.1016/j.compstruct.2020.111905
13. Asiri S (2022) Comparative modal analysis on fishing rod made of functionally graded composite material using finite element analysis. *J Appl Biomater Funct Mater* 20: 3. https://doi.org/10.1177/22808000221089774
14. Filippi M, Carrera E, Zenkour AM (2015) Static analyses of FGM beams by various theories and finite elements. *Compos B Eng* 72: 1–9. doi: 10.1016/j.compositesb.2014.12.004
15. Chakraborty A, Gopalakrishnan S, Reddy JN (2003) A new beam finite element for the analysis of functionally graded materials. *Int J Mech Sci* 45: 519–539. https://doi.org/10.1016/S0020-7403(03)00058-4
16. Yoon K, Lee P. S, Kim DN (2015) Geometrically nonlinear finite element analysis of functionally graded 3D beams considering warping effects. *Compos Struct* 132: 1231–1247. https://doi.org/10.1016/j.compstruct.2015.07.024
17. Costa DM, Loja MA (2017) Bat-inspired optimization of multilayered adaptive structures. *Compos Struct* 168: 189–215. https://doi.org/10.1016/j.compstruct.2017.01.067
18. Vallejos A, Ayala S, Arciniega R (2020) Improved first order formulation for buckling analysis of functionally graded beams. *2020 Congreso Internacional de Innovación y Tendencias en Ingeniería (CONIITI)* 1–6. https://doi.org/10.1109/CONIITI51147.2020.9240368
19. Bian PL, Qing H, Yu T (2022) A new finite element method framework for axially functionally-graded nanobeam with stress-driven two-phase nonlocal integral model. *Compos Struct* 295: 9. https://doi.org/10.1016/j.compstruct.2022.115769
20. Mota AF, Loja MA, Barbosa JI, er al. (2022) Mechanical behavior of a sandwich plate with aluminum foam core, using an image-based layerwise model. *Mech Adv Mater Struct* 29: 4074–4095. https://doi.org/10.1080/15376494.2021.1919801

21. Luo Y (2023) Voxel-based design and characterization of functionally graded materials. *Results Mater* 17: 3. https://doi.org/10.1016/j.rinma.2023.100375
22. Luu NG, Banh TT (2023) Static, dynamic and stability analysis of multi-dimensional functional graded plate with variable thickness using deep neural network. *Tech Rep* https://doi.org/10.48550/arXiv.2301.05900
23. Penna R, Feo L, Lovisi G, et al. (2022) Application of the higher-order hamilton approach to the nonlinear free vibrations analysis of porous fg nano-beams in a hygrothermal environment based on a local/nonlocal stress gradient model of elasticity. *Nanomater* 12: 2098. https://doi.org/10.3390/nano12122098
24. Penna R (2023) Bending analysis of functionally graded nanobeams based on stress-driven nonlocal model incorporating surface energy effects. *Int J Eng Sci* 189: 103887. https://doi.org/10.1016/j.ijengsci.2023.103887
25. Lovisi G (2023) Application of the surface stress-driven nonlocal theory of elasticity for the study of the bending response of fg cracked nanobeams. *Compos Struct* 324: 117549. https://doi.org/10.1016/j.compstruct.2023.117549
26. Loja M, Rzeszut K, Barbosa J (2022) Nonlocal free vibrations of metallic fgm beams. *J Compos Sci* 6: 125. https://doi.org/10.3390/jcs6050125
27. Giunta G, Crisafulli D, Belouettar S, et al. (2013) A thermo-mechanical analysis of functionally graded beams via hierarchical modelling. *Compos Struct* 95: 676–690. https://doi.org/10.1016/j.compstruct.2012.08.013
28. Qin Y, Li X, Yang E, et al. (2016) Flapwise free vibration characteristics of a rotating composite thin-walled beam under aerodynamic force and hygrothermal environment. *Compos Struct* 153: 490–503. https://doi.org/10.1016/j.compstruct.2016.06.057
29. Valencia Murillo C, Gutierrez Rivera M, Celaya Garcia L (2023) Thermal–structural linear static analysis of functionally graded beams using reddy beam theory. *Math Comput Appl* 28: 84. https://doi.org/10.3390/mca28040084
30. Tian J, Zhang Z, Hongxing H (2019) Free vibration analysis of rotating functionally graded double-tapered beam including porosities. *Int J Mech Sci* 150: 526–538. https://doi.org/10.1016/j.ijmecsci.2018.10.056
31. Mota A, Loja M, Barbosa J, et al. (2020) Porous functionally graded plates: an assessment of shear correction factor influence on static behavior. *Math Comput Appl* 25: 25. https://doi.org/10.3390/mca25020025
32. Akbas D, Fageehi Y, Assie A, et al. (2022) Dynamic analysis of viscoelastic functionally graded porous thick beams under pulse load. *Eng Comput* 38: 365–377. https://doi.org/10.1007/s00366-020-01070-3
33. Lee J, Lee B (2022) Coupled flexural-torsional free vibration of an axially functionally graded circular curved beam. *Mech Compos Mater* 57: 833–846. https://doi.org/10.1007/s11029-022-10003-8.
34. Özmen U, Özhan B (2022) Computational modeling of functionally graded beams: A novel approach. *J Vib Eng Technol* 10: 2693–2701. https://doi.org/10.1007/s42417-022-00515-x
35. Li Z, Xu Y, Huang D (2021) Analytical solution for vibration of functionally graded beams with variable cross-sections resting on pasternak elastic foundations. *Int J Mech Sci* 191: 106084. https://doi.org/10.1016/j.ijmecsci.2020.106084

36. Gaspar J, Loja M, Barbosa J (2023) Static and free vibration analyses of functionally graded plane structures. *J compos sci* 7: 377. https://doi.org/10.3390/jcs7090377
37. Loja MR, Barbosa J, Soares CM (1997) Buckling behaviour of laminated beam structures using a higher order discrete model. *Compos Struct* 38: 119–131. https://doi.org/10.1016/S0263-8223(98)80011-1
38. Carvalho A, Silva T, Loja M, et al. (2017) Assessing the influence of material and geometrical uncertainty on the mechanical behavior of functionally graded material plates. *Mech Adv Mater Struct* 24: 417–426. https://doi.org/10.1080/15376494.2016.1191100
39. Reddy JN (2003) *Mechanics of Laminated Composite Plates and Shells*, 2 Eds., CRC Press, Boca Raton.
40. Carvalho A (2023) Study of damping of bare and encased steel I-Beams using the thermoelastic model. *Buildings* 13: 2964. https://doi.org/10.3390/buildings13122964
41. Dassault Systèmes (2021) Solidworks. Available from: https://www.solidworks.com/.
42. Martha L (2018) Ftool-two-dimensional frame analysis tool. Available from: https://www.ftool.com.br/Ftool/.